Finite gyroradius effects in the electron outflow of asymmetric magnetic reconnection

C. Norgren, D. B. Graham, Yu. V. Khotyaintsev, M. André, A. Vaivads, L. -J. Chen, P. -A. Lindqvist, G. T. Marklund, R. E. Ergun, W. Magnes, et al.

AGU PUBLICATIONS

Geophysical Research Letters

RESEARCH LETTER
10.1002/2016GL069205

Special Section:
First results from NASA's Magnetospheric Multiscale (MMS) Mission

Finite gyroradius effects in the electron outflow of asymmetric magnetic reconnection

C. Norgren[1,2], D. B. Graham[1], Yu. V. Khotyaintsev[1], M. André[1], A. Vaivads[1], L.-J. Chen[3,4], P.-A. Lindqvist[5], G. T. Marklund[5], R. E. Ergun[6], W. Magnes[7], R. J. Strangeway[8], C. T. Russell[8], R. B. Torbert[9], W. R. Paterson[3], D. J. Gershman[3,4], J. C. Dorelli[3], L. A. Avanov[3], B. Lavraud[10,11], Y. Saito[12], B. L. Giles[3], C. J. Pollock[3], and J. L. Burch[13]

[1]Swedish Institute of Space Physics, Uppsala, Sweden, [2]Department of Physics and Astronomy, Uppsala University, Uppsala, Sweden, [3]NASA Goddard Space Flight Center, Greenbelt, Maryland, USA, [4]Department of Astronomy, University of Maryland, College Park, Maryland, USA, [5]Space and Plasma Physics, School of Electrical Engineering, KTH Royal Institute of Technology, Stockholm, Sweden, [6]Laboratory of Atmospheric and Space Physics, University of Colorado Boulder, Boulder, Colorado, USA, [7]Space Research Institute, Austrian Academy of Sciences, Graz, Austria, [8]Department of Earth and Space Sciences, University of California, Los Angeles, California, USA, [9]Space Science Center, University of New Hampshire, Durham, New Hampshire, USA, [10]Institut de Recherche en Astrophysique et Planétologie, Université de Toulouse, Toulouse, France, [11]Centre National de la Recherche Scientifique, UMR 5277, Toulouse, France, [12]Institute of Space and Astronautical Science, JAXA, Sagamihara, Japan, [13]Southwest Research Institute, San Antonio, Texas, USA

Key Points:
- An electron scale reconnecting current sheet is observed
- Crescent-shaped electron distributions are observed in the electron outflow
- The crescents are associated with finite electron gyroradius effects

Correspondence to:
C. Norgren,
cecilia.norgren@irfu.se

Citation:
Norgren, C., et al. (2016), Finite gyroradius effects in the electron outflow of asymmetric magnetic reconnection, *Geophys. Res. Lett.*, *43*, 6724–6733, doi:10.1002/2016GL069205.

Received 20 APR 2016
Accepted 9 JUN 2016
Accepted article online 13 JUN 2016
Published online 6 JUL 2016

Abstract We present observations of asymmetric magnetic reconnection showing evidence of electron demagnetization in the electron outflow. The observations were made at the magnetopause by the four Magnetospheric Multiscale (MMS) spacecraft, separated by ~15 km. The reconnecting current sheet has negligible guide field, and all four spacecraft likely pass close to the electron diffusion region just south of the X line. In the electron outflow near the X line, all four spacecraft observe highly structured electron distributions in a region comparable to a few electron gyroradii. The distributions consist of a core with $T_{\parallel} > T_{\perp}$ and a nongyrotropic crescent perpendicular to the magnetic field. The crescents are associated with finite gyroradius effects of partly demagnetized electrons. These observations clearly demonstrate the manifestation of finite gyroradius effects in an electron-scale reconnection current sheet.

1. Introduction

Magnetic reconnection is a fundamental plasma process in which the magnetic field topology changes and energy stored in the magnetic field is transferred to plasma particles, accelerating them. The changing magnetic field topology enables plasma transport across priorly closed boundaries and is a critical component in the Sun-Earth interaction, as well as in other astrophysical and laboratory plasmas [*Yamada et al.*, 2010]. Magnetic reconnection is a multiscale process, where ions and electrons decouple from the magnetic field at ion and electron scales, respectively, and form the ion and electron diffusion regions (EDR). At the magnetopause, where the plasma density and temperature change significantly between the magnetosheath and the magnetosphere, magnetic reconnection is asymmetric. The magnetic reconnection outflow is dominated by magnetosheath plasma, and the flow stagnation point is no longer colocated with the X line but is shifted toward the low-density magnetospheric side [*Cassak and Shay*, 2007]. This leads to an asymmetric outflow pattern, and as a result, the Hall magnetic field structure is modified, becoming more dipolar than quadropolar [*Pritchett*, 2008; *Tanaka et al.*, 2008; *Mozer et al.*, 2008; *Yoo et al.*, 2014].

Inside the EDR, where the length scale of magnetic field curvature can become comparable to the electron gyroradius ρ_e, the electrons become demagnetized and follow complicated trajectories. Where ρ_e is comparable to the length scale of gradients in plasma temperature and density, such motion enables mixing of different plasmas. In simulations, the electron distributions in the EDR have been shown to be highly structured and nongyrotropic [*Scudder and Daughton*, 2008; *Aunai et al.*, 2013; *Swisdak*, 2016]. Several simulations have observed crescent-shaped electron distributions in the direction perpendicular to the magnetic field that are related to finite gyroradius effects [*Hesse et al.*, 2014; *Bessho et al.*, 2014, 2016; *Chen et al.*, 2016]. How finite gyroradius effects and electron demagnetization manifest in reconnection in nature has hitherto been challenging to study, due to the small length and time scales involved. However, the Magnetospheric

Multiscale (MMS) mission [*Burch et al.*, 2015], launched in March 2015, provides unprecedented opportunities to observe high time resolution particle distributions and electromagnetic fields. Recent MMS observations of asymmetric magnetopause reconnection reported such effects manifested as crescent-shaped electron distributions on the low-density side of the X line [*Burch et al.*, 2016]. The crescents were perpendicular to the magnetic field and oriented in the same direction as the inferred X line, consistent with crescents observed in simulations. In this paper, we use MMS data to study the finite gyroradius effects in the electron outflow of a reconnecting current sheet close to the EDR.

2. Observations

We present an event from 16 October 2015, between 10:33:20 and 10:34:00, when the four MMS spacecraft make an outbound and inbound pass of the magnetopause, at [9.2, 7.5, −0.6] Earth radii in geocentric solar ecliptic (GSE) coordinates. We use data from the fast plasma investigation (FPI) [*Pollock et al.*, 2016], fluxgate magnetometer (FGM) [*Russell et al.*, 2014], and electric field double probes [*Lindqvist et al.*, 2014; *Ergun et al.*, 2014]. All the times stated in the paper are in coordinated universal time (UTC). MMS is in a tetrahedron formation, with a separation of ∼15 km. Therefore, they all observe similar plasmas and fields, albeit with slight time differences. Figure 1 presents an overview of the event, with a more detailed view of the outbound crossing where the spacecraft move from the magnetosphere to the magnetosheath (Figures 1f–1k), which is the focus of this paper. To more easily pinpoint the approximate times when the spacecraft tetrahedron passes between regions of different character, all quantities except the differential energy fluxes (Figures 1d–1e) and the electron agyrotropy (Figure 1k) are averaged over the four spacecraft. To see the differences observed by the different spacecraft, we refer to Figure 3, which will be discussed later. Throughout the paper, the vector data are presented in LMN coordinates, obtained from minimum variance analysis of **B** between 10:33:20 and 10:34:38; **L** = [0.14, 0.17, 0.98], **M** = [0.31, −0.94, 0.12], **N** = [0.94, 0.29, −0.18] (GSE).

The magnetopause is characterized by a large magnetic shear angle (Figure 1a, $\Delta B_L \sim 70$ nT, $B_M \sim B_N \sim 0$), is highly asymmetric (Figure 1b, $n_{\mathrm{MSP}}/n_{\mathrm{MSH}} \approx 20$), and has a high flow shear, as seen in the ion velocities, $v_{i,M}$ (Figure 1c). During the whole crossing $v_{i,L} < 0$. On the magnetospheric side before 10:22:23, $v_{i,L}$ is associated with a tenuous ion population (Figure 1d) traveling at pitch angle $\theta = 180°$ (not shown), i.e., antiparallel to **B**. This is likely due to open field lines connected to the magnetosheath at a distant northward reconnection X line. Further into the magnetosheath, $|v_{i,L}|$ decreases and is associated with a denser ion population that at around 10:33:30 is oriented mainly perpendicular to **B** (Figure 1, yellow shaded interval). This region is further characterized by large current densities **J** calculated from particle moments, which are highly structured, featuring reversals in J_L (Figure 1f). **J** is mainly carried by the electrons, as seen by comparing Figures 1f to 1g. Around this time, we also observe the largest value of the divergence of the electron pressure tensor $\nabla \cdot \mathbf{P_e}$ (Figure 1h). We calculate $\nabla \cdot \mathbf{P_e}$ using the four spacecraft and the full pressure tensor [*Paschmann and Daly*, 1998]; therefore, $\nabla \cdot \mathbf{P_e}$ is an average over the spacecraft tetrahedron. Parallel electron heating, $T_{\parallel} > T_{\perp}$, is observed on both the low-density and high-density side of the magnetopause (Figure 1i). Between these two regions of parallel heating, there is a region characterized by more isotropic distributions. *Lavraud et al.* [2016] found that the magnetic field curvature in this region was suffienctly large to scatter electrons down to 20 eV.

To investigate the electron dynamics in the region with enhanced current and low B_L, we look at the different force terms of the electron momentum equation:

$$m_e n_e \frac{\mathrm{d}\mathbf{v_e}}{\mathrm{d}t} = -e n_e(\mathbf{E} + \mathbf{v_e} \times \mathbf{B}) - \nabla \cdot \mathbf{P_e}. \quad (1)$$

Since $\nabla \cdot \mathbf{P_e}$ corresponds to a four-spacecraft average, we compare it to **E** and $\mathbf{v_e} \times \mathbf{B}$ averaged over the four spacecraft, using the electric field unit mV/m (Figure 1j). The terms are closely aligned with **N**, so we only show this component. In a large part of the region with enhanced current, the electric field in the electron bulk frame, $\mathbf{E'} = \mathbf{E} + \mathbf{v_e} \times \mathbf{B}$, is nonzero (Figures 1j and 3h) and approximately balanced by the divergence of the electron pressure: $\left|\mathbf{E} + \mathbf{v_e} \times \mathbf{B} + \frac{\nabla \cdot \mathbf{P_e}}{n_e e}\right|_N \lesssim 1$ mV/m (Figure 1j). The electron bulk motion thus deviate from the $\mathbf{E} \times \mathbf{B}$ drift, and effects related to plasma gradients are nonnegligible.

At ∼10:33:30, the length scale of the electron pressure divergence has a minimum of $L_P = \mathrm{Tr}(\mathbf{P_e})/3|\nabla \cdot \mathbf{P_e}| \sim$ 15km $\sim 10\rho_e$, where $\mathrm{Tr}(\mathbf{P_e})$ is the four spacecraft average. This suggests the layer is thin and that finite gyroradius effects are important, which may lead to mixing of plasmas of different regions. From a kinetic viewpoint, finite gyroradius effects can lead to agyrotropic particle distributions. To quantify this, we calculate

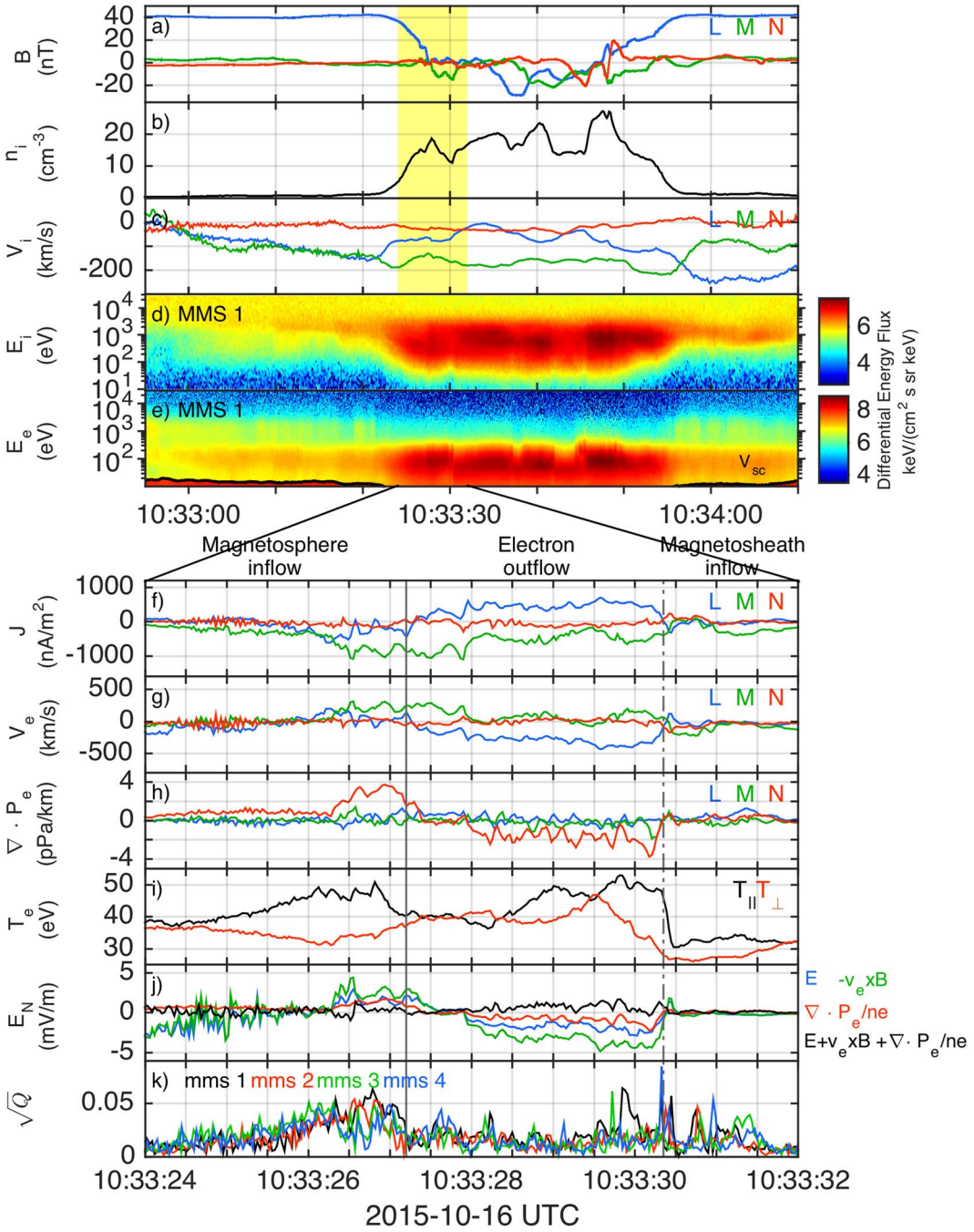

Figure 1. Overview of magnetopause crossing. All quantities, unless stated, are averaged over the four spacecraft. a) Magnetic field. b) Density. c) Ion bulk velocity. d) Ion and e) electron omnidirectional differential energy flux, observed by MMS1. f) Current density obtained from particle moments. g) Electron bulk velocity. h) Electron pressure divergence. i) Parallel and perpendicular electron temperatures. j) N components of the force terms from the electron momentum equation. k) Electron agyrotropy measure, $\sqrt{Q}$, observed by MMS1-4.

the measure of electron agyrotropy, $\sqrt{Q}$ [*Swisdak*, 2016] (similar to D_{ng} defined by *Aunai et al.* [2013]). Two regions of enhanced $\sqrt{Q}$ are discerned, around 10:33:27 and 10:33:30 (Figure 1k). The first region is highly anisotropic but has no outstanding features in the electron distributions in the plane perpendicular to **B**. In the second region, characterized by thinner peaks in $\sqrt{Q}$, all four spacecraft observe electron distributions that clearly show agyrotropic features. The time at which these distributions are observed coincide with the regions of large values of negative $v_{e,L}$ (Figures 1g and 3i) and small L_P.

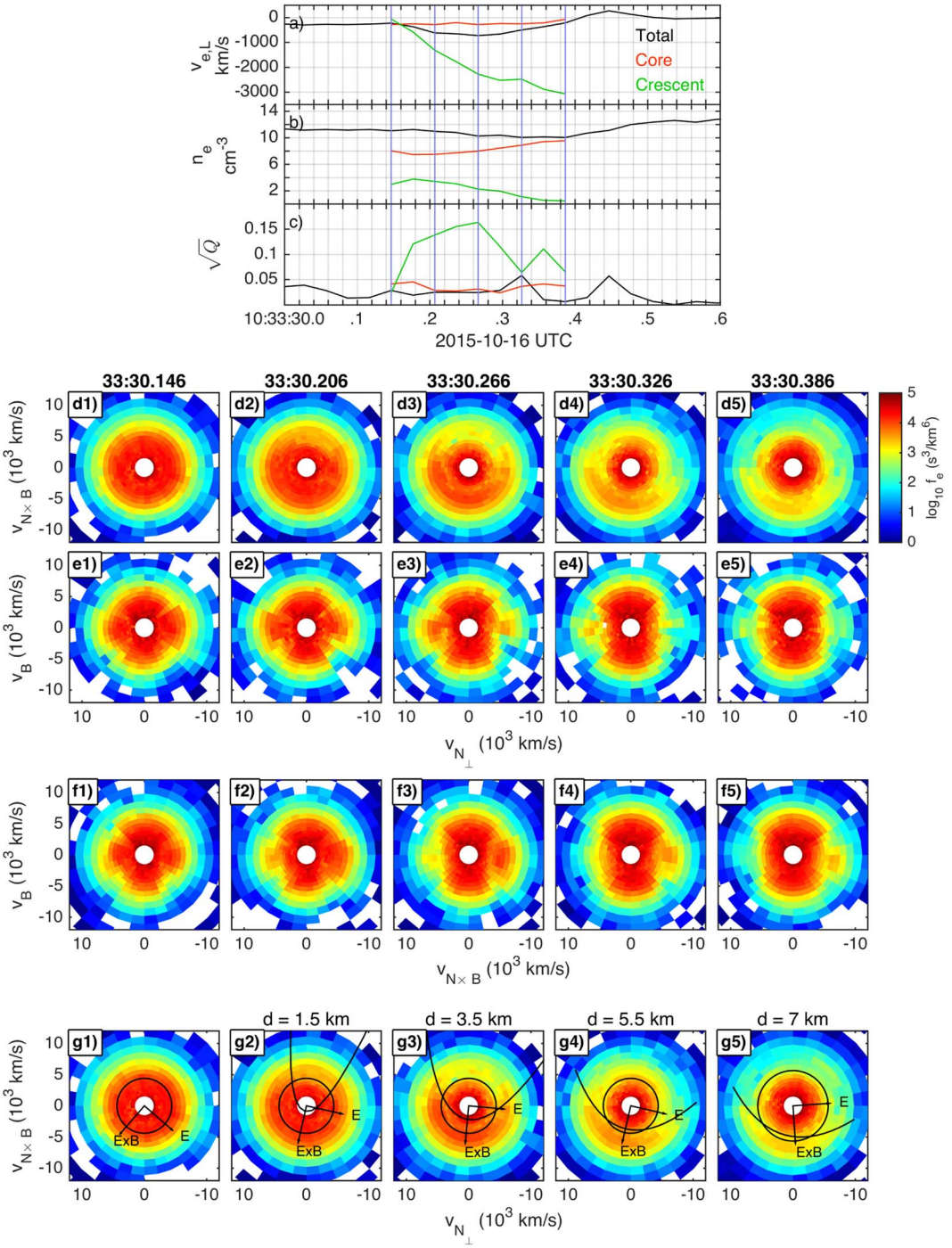

Figure 2. Properties and structure of electron distributions observed by MMS1 in a thin current layer. (a) Electron velocity $v_{e,L}$, (b) density, and (c) agyrotropy measure $\sqrt{Q}$ for the total distribution, the core, and the crescent, respectively. The vertical lines mark the times of the electron distributions shown in Figures 2d–2g. The projection of the electron distributions are made in planes perpendicular to (d) **B**, (e) **N** × **B**, and (f) $\mathbf{N}_\perp = \mathbf{B} \times (\mathbf{N} \times \mathbf{B})$. (g) The same plane as in Figure 2d but including the local **E** and **E** × **B** directions, as well as a fit to the lower bound of the crescent based on equation (2).

2.1. Kinetic Structure of Electron Distributions

In this subsection we investigate in detail the agyrotropic features of the electron distributions. We present observations by MMS1, which show a clear evolution in the electron distributions over a short time, 10:33:30.1–10:33:30.4, coinciding with the narrow peak in $v_{e,L}<0$ (Figures 2a and 3i). Similar distributions associated with $v_{e,L}<0$ are also observed by MMS2-MMS4 (not shown). Figures 2d–2f show orthogonal slices of the electron distribution at five different times indicated by vertical lines in Figures 2a–2c. The three planes are defined by the coordinate system: **B**—the local magnetic field direction, $\mathbf{N}\times\mathbf{B}$ ($\sim$**L**), and $\mathbf{N}_\perp=\mathbf{B}\times(\mathbf{N}\times\mathbf{B})$. Electrons within $\pm15°$ of each respective plane are included. FPI samples one 3-D electron distribution over 30 ms. Each distribution in Figure 2 corresponds to one such sample, and every second distribution is shown. The electron cyclotron frequency at this time is $f_{ce}\sim400$ Hz, $f_{ce}^{-1}\sim2.5$ ms.

The electron distributions consist of two populations: a core with $T_\parallel>T_\perp$ and a crescent-shaped population with $T_\perp>T_\parallel$ (Figures 2d–2f). The crescents are centered along $\sim\mathbf{E}\times\mathbf{B}\sim-\mathbf{L}$ (Figure 2g). As MMS1 crosses the velocity spike, we observe the following evolution in the crescent distribution with time: (1) the azimuthal extent decreases (Figure 2d), (2) the lower energy limit of the crescent increases while the upper bound of the crescent remains the same, $v_{max}\sim8000$ km/s (equivalent to $E_{max}\sim180$ eV), and (3) the range of pitch angles decreases Figures 2e and 2f. The fullest and faintest crescents cover the pitch angle ranges $\Delta\theta=75°$ and $\Delta\theta=45°$, respectively. The crescents observed by MMS2–MMS4 are less distinct than the ones observed by MMS1.

To follow and quantify the evolution of the crescent distributions, we estimate their moments. To isolate the crescents from the core, we set a lower energy bound (see circles in Figure 2g) and include only the range of pitch angles to which the core belong (centered at $\theta\approx90°$). The full azimuthal extent of the higher-energy part of the core centered at $\theta\approx90°$ is thus included in the crescent moments. We note that this increases the density and likely lowers the agyrotropy and bulk velocity with respect to the pure crescent. The partial moments show that the bulk velocity of the crescent distribution increases (Figure 2a) as its density decreases (Figure 2b) when the crescent become fainter. The velocity of the core is constant and smaller than the total bulk velocity; therefore, the peak in $v_{e,L}$ is due to the crescents. The crescents are thus responsible for the electron convection term of equation (1) in this region (Figures 1j). The agyrotropy of the core ($\sqrt{Q}<0.05$) is comparable to the agyrotropy of the total distribution. Therefore, although the crescents are clearly agyrotropic, $\sqrt{Q}_{max}=0.16$ (Figure 2c), their densities are too small to significantly increase the agyrotropy of the total distribution. Thus, in this case, large values of $\sqrt{Q}$ of the total electron distributions are not a good indicator of crescent-shaped distributions.

2.2. Current Sheet Structure

Now we investigate where the crescent distributions are located within the magnetopause by looking at properties of the fields and particle moments. We can distinguish three different regions, which are marked in Figures 1f–1k and 3 and separated by solid and dashed lines, respectively. We interpret the region with enhanced **J** as a reconnection current layer, and the three regions as the magnetospheric inflow region, the electron reconnection outflow, and the magnetosheath inflow region, respectively. We will validate this interpretation in the following paragraphs. The inferred spacecraft trajectory through the reconnection layer is below the X line and shown as a dashed line in Figures 4a and 4b. Figure 4a shows the out-of-plane magnetic field B_M and Figure 4b shows the electron bulk velocities $v_{e,L}$. The black solid lines show the in-plane magnetic field. The figures are from the 2-D simulation by *Chen et al.* [2016], and for further descriptions we refer to that paper.

The first region, before 10:33:27.20, is characterized by large but decreasing B_L. The first sign that we approach an active region is the appearance of waves around the lower hybrid frequency $f_{LH}\sim20$ Hz (Figures 1j and 3j). Adjacent to this region we observe an increasing $T_{||}$ (Figure 1i), as electrons are heated parallel to **B**. This heating is often observed in the magnetospheric inflow region of magnetic reconnection and is due to acceleration by parallel electric fields [*Egedal et al.*, 2011; *Graham et al.*, 2014, 2016]. Bridging this region of parallel heating but closer to the magnetosphere separatrix, we observe the bulk of the electron population moving toward the X line ($v_{e,L}>0$ in Figures 1g and 3i, and $v_{e,||}$ in Figure 3h), at the same time as an out-of-plane current density $J_M<0$ (Figures 1f and 3g) and magnetic field $B_M>0$ develops (Figures 1a and 3d). These signatures are consistent with the magnetospheric inflow region [*Pritchett*, 2008]. At the boundary of the magnetospheric inflow—at the magnetospheric separatrix (10:33:27.20)—we no longer observe any parallel heating, $T_{||}\sim T_\perp$, and the electron bulk velocities $v_{e,L}$ changes direction.

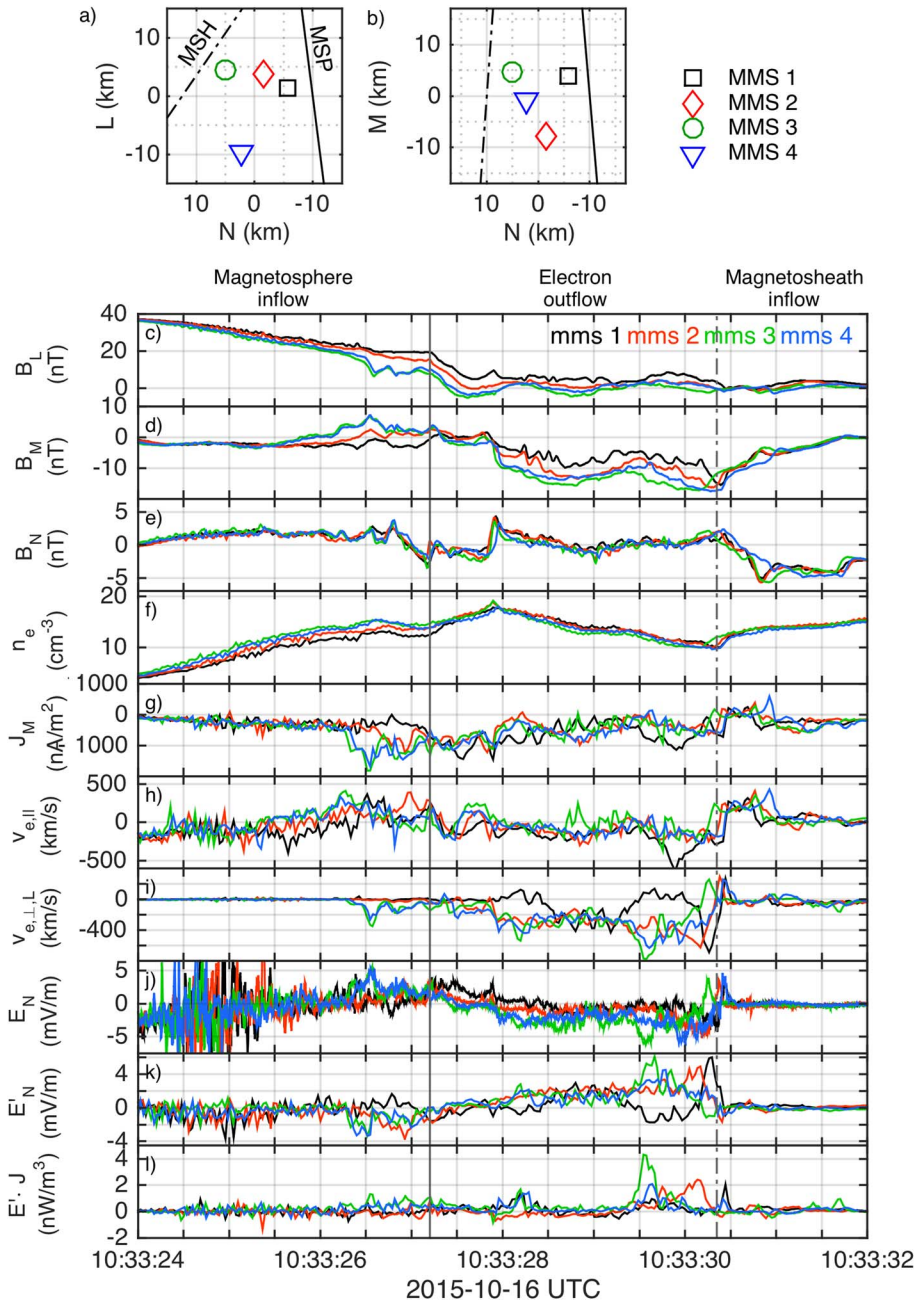

Figure 3. Detailed structure of the current sheet as seen by the four spacecraft. Spacecraft configuration in (a) N-L plane and (b) N-M plane. The black solid and dashed lines indicate the magnetosphere and magnetosheath boundary orientation, respectively, obtained from timing analysis. Magnetic field (c) B_L, (d) B_M, and e) B_N. (f) Electron density. (g) Current density J_M derived from electron and ion moments. (h) Electron velocity parallel to **B**. (i) Perpendicular electron velocity $v_{\perp,L}$. (j) Electric field E_N. (k) Electric field in the electron bulk frame, $E'_N = E_N + (\mathbf{v_e} \times \mathbf{B})_N$. (l) Electron frame energy dissipation, $\mathbf{E'} \cdot \mathbf{J}$.

In the second region, 10:33:27.20–10:33:30.35, the bulk of the electron population now moves away from the X line perpendicular to **B**, $v_{e,\perp,L} < 0$. The out-of-plane magnetic field changes direction to $B_M < 0$ a little bit inside the separatrix. The structure of B_M in the two regions is consistent with the Hall magnetic field below the X line in Figure 4a. The peak of $v_{e,\perp,L} < 0$ occurs toward the end of this region and is characterized by the agyrotropic crescent-shaped distributions described in section 2.1. The signatures described above are consistent with this region being the electron reconnection outflow. At the outer boundary of the outflow region—at the magnetosheath separatrix—we observe a density cavity associated with a sharp reversal in $v_{e,\perp,L}$ and a large drop in electron temperature.

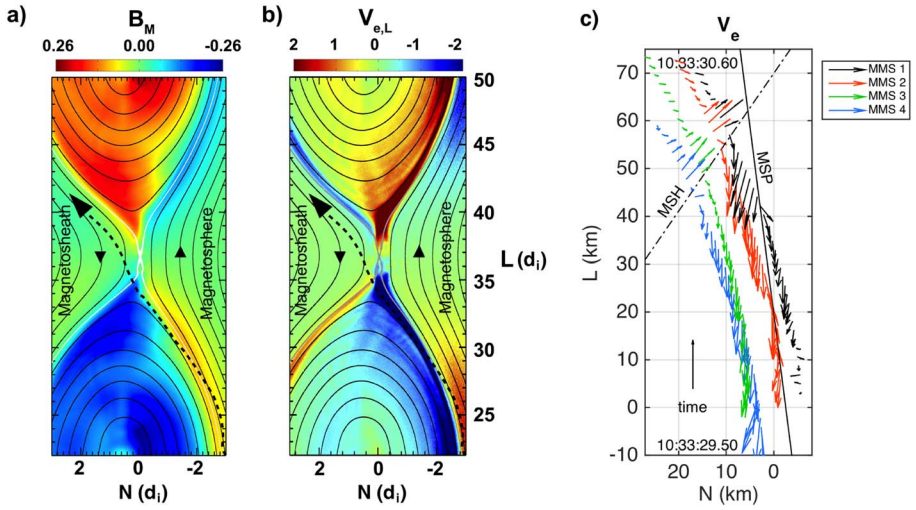

Figure 4. (a and b) Spacecraft trajectory (dashed line) through an asymmetric reconnection layer. Black solid lines show the in-plane magnetic field. Shown in Figure 4a is the out-of-plane Hall magnetic field, B_M. Shown in Figure 4b is the in-plane electron velocities, $v_{e,L}$. The figures are from the simulation by *Chen et al.* [2016]. (c) Electron velocities in LN plane observed 10:33:29.50 (bottom) – 10:33:30.60 (top). The solid and dashed lines mark the orientation of the magnetospheric and magnetosheath boundary, respectively, at the limits of the electron outflow.

In the third region, after the electron velocity reversal, the bulk electron motion is thus toward the X line (Figure 4b), consistent with magnetosheath inflow. The motion of the electrons in this layer is initially aligned perpendicular to **B**, which is dominated by the Hall field B_M. As the remaining B_M trails off across the boundary, the electron motion becomes more field aligned. After ~ 10:33:31.00, the spacecraft enter the magnetosheath where the electron distributions become approximately isotropic. Low |**B**| and |**E**| are observed for a few seconds, before B_L becomes largely negative at around 10:33:38.

We conclude that the crescent-shaped distributions are found in the region of electron outflow, where they constitute the peak of the electron jet.

3. Discussion

During this magnetopause crossing, we believe MMS passes close to, or inside, a reconnection EDR. All of the spacecraft observe a direct transition from the outflow to the magnetosheath inflow at the sharp reversal in $v_{e,L}$ around the magnetosheath separatrix (dashed line in Figures 1f–1k and 3). In simulations, this direct transition only occurs inside or close to the EDR. Further downstream, the electron outflow is expected to become more field aligned and is predominantly located to the magnetospheric side of the outflow region [*Chen et al.*, 2016; *Khotyaintsev et al.*, 2016].

To investigate the topology of the reconnection layer in more detail, we perform timing analysis of the fields and particle moments. Timing analysis of B_L in the outer magnetospheric inflow region (10:33:25.5) provides the boundary normal velocity $\mathbf{v_{n,MSP}} \approx 32 \times [-0.05, -0.08, 1.00]$ km/s (LMN). Still in the magnetospheric inflow, but closer to the separatrix, 10:33:26.2–10:33:27.8, B_L temporarily forms a plateau, as the boundary velocity decreases to $v_{MSP} \sim 10$ km/s. At the magnetosheath separatrix, timing analysis of n_e, B_M, $v_{e,\perp,L} > 0$, and $E_N > 0$ each give a boundary normal velocity $\mathbf{v_{n,MSH}} \approx 55 \times [-0.50, -0.10, -0.86]$ km/s (LMN). MMS1 observes the large negative $v_{e,L}$ for about 0.25 s. Based on this, we estimate the thickness of the electron outflow $w \sim 0.25 v_{n,MSH}$ to be not larger than 15 km, comparable to the pressure length scale L_P. In comparison, $\rho_e \approx 1.5$ km, and the electron inertial length $d_e \approx 1$ km. The orientation of the magnetospheric and magnetosheath side boundary planes is shown as black solid and dashed lines in Figures 3a and 3b.

To illustrate the flow structure close to $|\mathbf{v}_{e,L}|_{max}$ and the magnetosheath separatrix, we plot $\mathbf{v_e}$ in the time interval 10:33:29.50–10:33:30.60 (Figure 4c). In this figure, the magnetosheath and magnetospheric side boundaries has been placed at the edges of $\mathbf{v_{e,L}} < 0$ as observed by MMS1. On the magnetosheath side, all four spacecraft observe $\mathbf{v_e}$ that is tangential and **E** that is normal to the boundary (not shown), respectively. This suggests the boundary is roughly planar over the tetrahedron volume. The planes form an angle of 34°,

suggesting a widening of the electron outflow away from the X line. However, we cannot determine the boundary orientation outside the spacecraft tetrahedron and therefore not decide the X line location. The motion of the spacecraft normal to the boundaries is based on $v_{n,\mathrm{MSP}}$ and $v_{n,\mathrm{MSH}}$. The motion tangential to the boundaries cannot be inferred from the timing, but there are clear indications that they are non zero, and by comparing the observations by the individual spacecraft, we are able to set some constraints. On the magnetosheath side, we have added a tangential velocity $\mathbf{v_{t,MSP}} = \mathbf{M}\times\mathbf{v_{n,MSH}}/|\mathbf{v_{n,MSH}}| \times 40$ km/s, such that the spacecraft motion close to this boundary is given by $\mathbf{v_{MSH}} = \mathbf{v_{n,MSH}} + \mathbf{v_{t,MSH}}$. The trajectories of MMS1, MMS2, and MMS3/MMS4 then form separate groups, consistent with the observed durations of $v_{e,L} < 0$ and the reversal to $v_{e,L} > 0$ (Figure 3i). This velocity is then projected on to the magnetospheric side boundary as $\mathbf{v_{t,MSP}} = \mathbf{M}\times\mathbf{v_{n,MSP}}/|\mathbf{v_{n,MSP}}| \times 60$ km/s. We note that the normal velocities on the magnetospheric side seem to be low during an extended period, as MMS1 observes signatures different to the other three spacecraft (Figure 3). We conclude that the inferred trajectories place MMS1 closest to the EDR. This is consistent with MMS1 observing the smallest Hall magnetic fields (B_M) and the thinnest outflow region ($v_{e,L}$). In a region this thin, with low **B**, electrons are expected to become partially demagnetized.

Now we investigate how the crescent-shaped electron distributions observed in the electron outflow develop. The orientation of the local magnetic field, $B_M \approx -10$ nT, gives counter clockwise electron gyro orbits in Figures 2d, 2g, 3a, and 4 (**B** is out of plane in these figures). Since the electrons constituting the crescents travel mainly along $-\mathbf{L}$ (Figure 2d), the instantaneous gyrocenters are on average located in the $-\mathbf{N}$ direction relative to the spacecraft, toward the low-density side of the reconnection layer. The dropout of lower energy electrons toward the magnetosheath places the origin of the crescent population toward the magnetosphere because only the highest energy electrons, which have the largest gyroradius, reach the location where the faintest crescent is sampled. This is consistent with the above timing analysis, which places the faintest crescent closer to the magnetosheath, and the fullest crescent closer to the magnetosphere. The local gyroradius of the highest energy electrons in the crescent (E=180 eV, $B_M = -10$ nT) is $\rho_{e,\mathrm{max}} = 4.5$ km. Since $\rho_{e,\mathrm{max}}$ is comparable to w, the electrons may observe varying **B** along their trajectories. If the electrons constituting the crescent cross into the region where $B_M > 0$ or even further to where $B_L > 0$, their trajectories will become meandering, and the electrons can be considered partly demagnetized.

The observed crescents are similar to distributions recently observed in magnetopause reconnection by *Burch et al.* [2016] and simulations of asymmetric reconnection [*Hesse et al.*, 2014; *Chen et al.*, 2016; *Bessho et al.*, 2016]. In both the observations and simulations, the crescents are predominantly found on the low-density side of the X line directed along **M** (coinciding with the local $\mathbf{E}\times\mathbf{B}$ direction). The crescents constitutes electrons that cross the magnetic field reversal in B_L from the high-density side and undergo partial gyro orbits into the low-density side of the X line. Although we observe the crescents in the electron outflow, toward the high-density (magnetosheath) side of the reconnecting current layer, and the dominant magnetic field is B_M instead of B_L, the formation mechanisms are likely similar. Assuming this, we follow *Bessho et al.* [2016] (their equation 7) and estimate the lower velocity bound of the crescent distribution to be:

$$v_{\perp 1} \geq \frac{v_{\perp 2}^2}{\omega_{\mathrm{ce}}}\frac{1}{d} - \frac{\omega_{\mathrm{ce}}}{4}d - \frac{|\mathbf{E}\times\mathbf{B}|}{B^2} \tag{2}$$

where $v_{\perp 1}$ and $v_{\perp 2}$ are aligned with $\mathbf{E}\times\mathbf{B}$ and **E**, respectively, and d is the distance along **E** to the turning point of the meandering trajectories, $B_M = 0$. This equation assumes linear variation of **B** along the direction of d and thus a spatially varying gyroradius. This lower boundary curve is parabolic and provides a reasonable boundary between the core and the crescent populations (Figure 2g), giving $d = 1-7$ km or a few $\rho_e \sim 1.5$ km. This is comparable to the distance between MMS1 and the magnetospheric side boundary of the outflow region in Figure 4c. The comparison between our observations and theoretical predictions supports the interpretation that the crescent distributions likely form by meandering trajectories of partially demagnetized electrons in a region where the electron gyroradius is comparable to the length scale of magnetic field gradients.

Since the distribution at 10:33:30.146 (Figures 2d1–2f1) with azimuthal extent ~360° constitutes electrons of all gyrophases, we consider this as close to the source of the crescent. However, we note that the distribution at this time is not completely isotropic and that the core and the perpendicular distribution are still distinguishable in the pitch angles. The maximum energy of the perpendicular distribution is slightly higher than the maximum energy of the parallel core, and both are well below the energy of magnetospheric electrons, $E \gtrsim 500$ eV (Figure 1e). Therefore, both populations likely originate from magnetosheath electrons.

The core population with $T_{||} > T_{\perp}$, which is observed both in the inflow and outflow, may have been heated in the inflow regions [*Egedal et al.*, 2011; *Graham et al.*, 2014, 2016; *Lavraud et al.*, 2016] without being significantly scattered perpendicular to **B** while crossing the separatrices. The perpendicular population, which is the origin of the crescent, may develop from magnetosheath electrons passing through the EDR and being heated perpendicular to **B** [*Bessho et al.*, 2014; *Lavraud et al.*, 2016]. The finite gyroradius effects forming the crescents appear due to the sharp electron scale boundary between the two plasmas described above.

To provide an indication of the energy dissipation associated with the crescent distributions, we calculate the energy dissipation in the electron frame of reference, $\mathbf{E}' \cdot \mathbf{J}$ (assuming charge neutrality) [*Zenitani et al.*, 2011] (Figure 3l). All four spacecraft except MMS1 observe a significant enhancement in $\mathbf{E}' \cdot \mathbf{J} > 0$ around the time of the southward electron jet when the crescents are observed. Nevertheless, this provides some indication that the electrons constituting the crescents can be accelerated in this region. Since the acceleration only affects the electrons during a certain gyrophase, it can be nonadiabatic. To estimate the average energy gain per gyro orbit, we calculate $\mathbf{E}' \cdot \mathbf{J}/n_e f_{ce}$. For MMS2, the maximum value is 3 eV ($\mathbf{E}' \cdot \mathbf{J} = 2$ nW/m^3, f_{ce}=400 Hz, $n_e = 11\text{cm}^{-3}$), which is about 7% of T_e (Figure 1i). Therefore, over multiple gyro orbits, the electrons may gain a significant amount of energy.

4. Conclusions

We investigate a magnetopause crossing with strong gradients in magnetic field and plasma parameters on a scale comparable to the spacecraft separation ~ 15 km. We find a region of strong current primarily carried by electrons. In this region, the divergence of the electron pressure is sufficiently large that electrons are not frozen in to the magnetic field. The electric field in the frame of the electron bulk flow is nonzero and balanced by the pressure divergence term. The observed magnetic field structure and electron flows indicate that MMS crossed a reconnection region close to the electron diffusion region. By examining the electron distributions in these regions, we find that the electron outflow is associated with pronounced crescent-shaped distributions in the plane perpendicular to the magnetic field. The crescents support the bulk electron flow constituting the outflow jet. While the isolated crescents are highly agyrotropic, their density is too low to significantly contribute to the agyrotropy of the complete distribution. The crescent population originates from magnetosheath electrons that has been heated perpendicular to the magnetic field, possibly when passing the electron diffusion region. The crescents form due to finite electron gyroradius effects across the magnetosheath separatrix. The crescents are thus a clear manifestation of finite gyroradius effects in an electron-scale reconnection current sheet.

Acknowledgments
We thank the entire MMS team and instrument PIs for data access and support. MMS data are available at https://lasp.colorado.edu/mms/sdc/public. This work was supported by the Swedish National Space Board, grants 23/12:2 and 175/15. The IRAP contribution was supported by CNES and CNRS. C.N. thanks the International Space Science Institute (ISSI) for supporting the team "from Cluster to MMS", from which this work was partly developed.

References

Aunai, N., M. Hesse, and M. Kuznetsova (2013), Electron nongyrotropy in the context of collisionless magnetic reconnection, *Phys. Plasmas*, *20*(9), 92903, doi:10.1063/1.4820953.

Bessho, N., L.-J. Chen, J. R. Shuster, and S. Wang (2014), Electron distribution functions in the electron diffusion region of magnetic reconnection: Physics behind the fine structures, *Geophys. Res. Lett.*, *41*, 8688–8695, doi:10.1002/2014GL062034.

Bessho, N., L.-J. Chen, and M. Hesse (2016), Electron distribution functions in the diffusion region of asymmetric magnetic reconnection, *Geophys. Res. Lett.*, *43*, 1828–1836, doi:10.1002/2016GL067886.

Burch, J. L., T. E. Moore, R. B. Torbert, and B. L. Giles (2015), Magnetospheric multiscale overview and science objectives, *Space Sci. Rev.*, *199*, 5–21, doi:10.1007/s11214-015-0164-9.

Burch, J. L., et al. (2016), Electron-scale measurements of magnetic reconnection in space, *Science*, *352*(6290), aaf2939, doi:10.1126/science.aaf2939.

Cassak, P. A., and M. A. Shay (2007), Scaling of asymmetric magnetic reconnection: General theory and collisional simulations, *Phys. Plasmas*, *14*(10), 102114, doi:10.1063/1.2795630.

Chen, L.-J., M. Hesse, S. Wang, N. Bessho, and W. Daughton (2016), Electron energization and structure of the diffusion region during asymmetric reconnection, *Geophys. Res. Lett.*, *43*, 2405–2412, doi:10.1002/2016GL068243.

Egedal, J., A. Le, P. L. Pritchett, and W. Daughton (2011), Electron dynamics in two-dimensional asymmetric anti-parallel reconnection, *Phys. Plasmas*, *18*(10), 102901, doi:10.1063/1.3646316.

Ergun, R. E., et al. (2014), The axial double probe and fields signal processing for the MMS mission, *Space Sci. Rev.*, *199*, 167–188, doi:10.1007/s11214-014-0115-x.

Graham, D. B., Y. V. Khotyaintsev, A. Vaivads, M. André, and A. N. Fazakerley (2014), Electron dynamics in the diffusion region of an asymmetric magnetic reconnection, *Phys. Rev. Lett.*, *112*(21), 215004, doi:10.1103/PhysRevLett.112.215004.

Graham, D. B., et al. (2016), Electron currents and heating in the ion diffusion region of asymmetric reconnection, *Geophys. Res. Lett.*, *43*, 4691–4700, doi:10.1002/2016GL068613.

Hesse, M., N. Aunai, D. Sibeck, and J. Birn (2014), On the electron diffusion region in planar, asymmetric, systems, *Geophys. Res. Lett.*, *41*, 8673–8680, doi:10.1002/2014GL061586.

Khotyaintsev, Y. V., et al. (2016), Electron jet of asymmetric reconnection, *Geophys. Res. Lett.*, *43*, doi:10.1002/2016GL069064.

Lavraud, B., et al. (2016), Currents and associated electron scattering and bouncing near the diffusion region at Earth's magnetopause, *Geophys. Res. Lett.*, *43*, 3042–3050, doi:10.1002/2016GL068359.

Lindqvist, P.-A., et al. (2014), The spin-plane double probe electric field instrument for MMS, *Space Sci. Rev.*, *199*, 137–165, doi:10.1007/s11214-014-0116-9.
Mozer, F. S., V. Angelopoulos, J. Bonnell, K. H. Glassmeier, and J. P. McFadden (2008), THEMIS observations of modified Hall fields in asymmetric magnetic field reconnection, *Geophys. Res. Lett.*, *35*, L17S04, doi:10.1029/2007GL033033.
Paschmann, G., and W. D. Daly (Eds.) (1998), *Analysis Methods for Multi-Spacecraft Data, ISSI Sci. Rep. SR-001*, The International Space Science Institute.
Pollock, C., et al. (2016), Fast plasma investigation for magnetospheric multiscale, *Space Sci. Rev.*, *199*, 331–406, doi:10.1007/s11214-016-0245-4.
Pritchett, P. L. (2008), Collisionless magnetic reconnection in an asymmetric current sheet, *J. Geophys. Res.*, *113*, A06210, doi:10.1029/2007JA012930.
Russell, C. T., et al. (2014), The magnetospheric multiscale magnetometers, *Space Sci. Rev.*, *199*, 189–256, doi:10.1007/s11214-014-0057-3.
Scudder, J., and W. Daughton (2008), "Illuminating" electron diffusion regions of collisionless magnetic reconnection using electron agyrotropy, *J. Geophys. Res.*, *113*, A06222, doi:10.1029/2008JA013035.
Swisdak, M. (2016), Quantifying gyrotropy in magnetic reconnection, *Geophys. Res. Lett.*, *43*, 43–49, doi:10.1002/2015GL066980.
Tanaka, K. G., et al. (2008), Effects on magnetic reconnection of a density asymmetry across the current sheet, *Ann. Geophys.*, *26*, 2471–2483, doi:10.5194/angeo-26-2471-2008.
Yamada, M., R. Kulsrud, and H. Ji (2010), Magnetic reconnection, *Rev. Modern Phys.*, *82*, 603–664, doi:10.1103/RevModPhys.82.603.
Yoo, J., M. Yamada, H. Ji, J. Jara-Almonte, C. E. Myers, and L.-J. Chen (2014), Laboratory study of magnetic reconnection with a density asymmetry across the current sheet, *Phys. Rev. Lett.*, *113*, 95002, doi:10.1103/PhysRevLett.113.095002.
Zenitani, S., M. Hesse, A. Klimas, and M. Kuznetsova (2011), New measure of the dissipation region in collisionless magnetic reconnection, *Phys. Rev. Lett.*, *106*(19), 195003, doi:10.1103/PhysRevLett.106.195003.